

Available online at www.sciencedirect.com

jmr&t
Journal of Materials Research and Technology

journal homepage: www.elsevier.com/locate/jmrt**Review Article**

Effect of 1wt.%Bi addition on microstructure and mechanical property of Mg–3Al alloy by twin roll casting and hot rolling



Hui Yu ^{a,*}, Ya Liu ^a, Yu Liu ^a, Dongliang Wang ^a, Yuling Xu ^b,
Binan Jiang ^c, Weili Cheng ^d, Weineng Tang ^b, Fuxing Yin ^e, Wei Yu ^{f,**}

^a School of Materials Science and Engineering, Tianjin Key Laboratory of Materials Laminating Fabrication and Interfacial Controlling Technology, Hebei University of Technology, Tianjin 300130, China

^b Baosteel Metal Co., Ltd., Shanghai 200940, China

^c PLA AAAAD, Hefei 230031, China

^d School of Materials Science and Engineering, Taiyuan University of Technology, Taiyuan 030024, China

^e Institute of New Materials, Guangdong Academy of Sciences, Guangzhou 510650, China

^f School of Materials Science and Engineering, Hefei University of Technology, Hefei 200039, China

ARTICLE INFO**Article history:**

Received 18 November 2022

Accepted 9 March 2023

Available online 14 March 2023

ABSTRACT

The microstructural evolution and mechanical properties of twin-roll casting (TRC) and hot rolling (HR) Mg–3Al–1Bi (in wt.%, TRC-AB31 and HR-AB31) alloys were investigated and compared with AZ31 alloy as the benchmark. The addition of Bi in TRCed alloys can not only reduce the central segregation but also introduce thermally stable Mg₃Bi₂ phases distributed uniformly in the α -Mg matrix. The second phases with a larger size lead to particle stimulated nucleation (PSN), which in turn, promoted the dynamic recrystallization (DRX) in HR-AB31 alloy and weaken its basal texture. The second phases play two different roles in AB31 alloy, on the one hand, the grain refinement and uniform microstructure resulted from enhanced DRX by second particles which retarding dislocation movement as well as inhibition of grain growth. On the other hand, such brittle particles can also act as the cracking source and degrade elongation. The strengthening mechanism of both AZ31 and AB 31 alloys is discussed and investigated.

© 2023 The Author(s). Published by Elsevier B.V. This is an open access article under the CC BY-NC-ND license (<http://creativecommons.org/licenses/by-nc-nd/4.0/>).

1. Introduction

With the increasingly serious energy concern and the raising demand for lightweight, the development of new weight-

saving and environmentally friendly materials becomes more and more urgent [1]. As the main source of carbon dioxide emissions, the automotive industry is keen to pursue such a target for that. Especially utilization of light and high

* Corresponding author.

** Corresponding author.

E-mail addresses: huiyu@vip126.com (H. Yu), yuwei52213@163.com (W. Yu).

<https://doi.org/10.1016/j.jmrt.2023.03.068>

2238-7854/© 2023 The Author(s). Published by Elsevier B.V. This is an open access article under the CC BY-NC-ND license (<http://creativecommons.org/licenses/by-nc-nd/4.0/>).

strength materials as structural components can significantly reduce the total weight of the vehicle [2], to reduce energy consumption. Magnesium (Mg) alloys with low density, as well as shock reduction, are considered as the most promising candidate material to achieve the above goal [3,4].

Recently, the application of twin-roll casting (TRC) on magnesium and its alloys has caused wide concern. The TRC process is known for its simplicity of processing and lower cost compared with direct chill ingot casting [43], which allows manufacturing sheet or strip products directly from a molten state. At present, many scholars have verified the effectiveness of the TRC process. Suk Bong Kang et al. [5] examined the microstructure evolution of TRCed Mg–3Al–0.5Mn–0.2Mm (AM30 + 0.2Mm) alloy strips, and the TRC sheets had superior yield and tensile strengths to ingot cast (IC) samples. J.H. Bae et al. [6] studied the segregation of Mg–3Al–1Sn (AT31) alloy with a narrow freezing range to reduce segregation defects. Suk Bong Kang et al. [7] investigated the microstructural evolution and mechanical properties of TRCed Mg–3.3Al–0.8Mn–0.2Ca (AM31 + 0.2Ca) alloy strips during warm rolling and subsequent annealing. These previous researches showed that the TRC process has a beneficial effect on microstructure and mechanical properties.

For improving strength and formability, some literature has shown that [8] can be achieved by adjusting the basal texture and activating other slip systems. The application of severe plastic deformation (SPD) methods, such as equal channel angular extrusion (ECAP) [9,10], high pressure torsion (HPT) [11], multidirectional forging (MDF) [12], multi-pass rolling [13,14] and continuous extrusion [15,16], are proved to weaken the basal texture and enhanced related ductility. In addition, the basal texture can also be modified by adding specific elements [17,18], i.e., rare earth (RE) elements [19]. Chino et al. [20] studied the tensile properties of Mg–1.5Zn–0.2Ce alloy rolled at 723 K and found that the synergistic effect of Ce addition and high rolling temperature weakened the texture intensity. However, the high cost and scarce resources of RE elements cut down the large-scale commercial application. To solve this problem, researchers gradually focus on Mg alloys with low content of RE or even no use of RE. Yuasa et al. [21] reported that the addition of Group II elements (Ca, Sr and Ba) can reduce the texture intensity too. According to the first principle calculation, the unstable stacking fault energy of prismatic $\langle a \rangle$ dislocation slip decreases more than basal $\langle a \rangle$ dislocation slip by adding such elements, and the formability increases with a decrease of atomic numbers. The extruded Mg–xAl–ySn–0.3Mn ($x = 1, 3, 6$; $y = 1, 3$) alloys [22] show bimodal structure composed of fine dynamic recrystallized (DRXed) grains and a high proportion of coarse deformed grains, exhibited yield strength (YS) more than 250 MPa and elongation of 20%. A very high strength Mg–8Al–4Sn–2Zn–0.15Mn was also developed (YS: 371 MPa, UTS: 415 MPa, and El.: 9.1%) [23]. Similar to RE elements, the main strengthening mechanism can be attributed to the joint effects of grain refinement, precipitation strengthening, and solid solution strengthening.

Recently, more and more studies have shown that RE-free Mg–Bi based [24,25] alloys and Mg alloys with minor Bi

addition [26,27] can obtain high performance upon rolling or extrusion. Rare literature reported Bi containing Mg alloy fabricated by twin-roll casting (TRC). Thus, this study mainly focused on the deformation behavior, microstructural evolution, and mechanical properties of Mg–3Al alloy with 1wt.%Bi addition (AB31), and compared with widely used Mg–3Al–1Zn (AZ31) alloy.

2. Experimental procedure

Pure Mg, Al, Bi, and Zn (all in 99.9 wt.%) were melted in the vacuum induction melting furnace under the protection of mixed CO₂ and SF₆ gas. When the metal is completely melted, it is transferred into a calcium silicate nozzle preheated to 650 °C and fed into a water-cooled copper-beryllium roller with a roller gap is 2 mm and a roller speed is 7.6 m/min. The TRCed plates with 60 mm in width and 3–4 mm in thickness are successfully produced and the corresponding chemical composition is shown in Table 1. Then, the TRCed strips were cut into 50 mm length and homogenized at 400 °C and held for 12 h. The T4 treatment uses a box-type (KSL-1100X) resistance furnace fitted with an inlet and outlet port at which argon is used as a protective gas to prevent burn on the alloy surface. After T4 treatment, followed by 3-pass hot rolling at 250 °C with controlled thickness reduction between 20 and 25%. To eliminate the residual stress and prevent edge cracking, the sheets were annealed at 400 °C for 1 h before the final pass and the eventual thickness of the hot-rolled (HR) sheets was 1 mm.

All the samples are ground, polished, and etched for microstructure characterization. Details of sample preparation can be found in our previous report [42]. The microstructure observation of these specimens was conducted on the optical microscope (OM: OLYCLA M3) and a scanning electron microscope (SEM: JSM-6510A). The phases in alloys were indexed by X-ray diffractometry (XRD: Smart Lab) using a scan range from 10° to 90° with a scan speed of 6°/min. Electron probe microanalysis (EPMA: JXA 8530F) was also used to accurately measure the segregation in TRCed alloys. The as-rolled Mg plates were analyzed by electron backscatter diffraction (EBSD: JEOL-JSM-7000F) along the rolling direction (RD). The samples were carefully grounded, punched, and jet-polished and the precipitates identification and dislocation analysis were performed on transmission electron microscope analysis (TEM: Tecnai F30). Moreover, for tensile tests, the samples cut from TRCed and HRed plates along the RD and the universal test machine (AGS-X and CMT6104) was used to carry out according to GB/T 228 standard (sample specification: 25 mm length, 6 mm width, 3 mm thickness) and ASTM B557M standard (20.6 mm length, 6.4 mm width, 1 mm thickness).

Table 1 – Chemical composition of TRCed AZ31 and AB31 alloys (mass fraction, %).

Alloy (wt.%)	Mg	Al	Zn	Bi	Si
AZ31	Bal.	3.23	1.010	—	0.161
AB31	Bal.	2.87	—	0.968	0.130

3. Results and discussion

3.1. Microstructure characterization

To understand about central segregation of plates produced by TRC, the equilibrium phase diagrams of Mg–3Al–1Zn and Mg–3Al–1Bi alloys were calculated by Pandat™ software. As shown in Fig. 1, the solidus temperature of both alloys decreases with the increase of Al element content. When the Al content is 3% (the red dotted line), the solidus temperatures of AZ31 and AB31 alloys are 510 ± 5 °C and 590 ± 5 °C, respectively. The prediction implies that the addition of Bi increases the solidification temperature and shortens the solidification range of Mg–Al alloys. Since the solidification of the alloy only occurs in a specific interval, the reduction of the solidification interval can reduce the hot cracking tendency and increase the fluidity. In other words, Bi addition can reduce the segregation tendency of TRCed Mg alloy to a certain extent. In addition, when the temperature drops to 310 ± 5 °C, the Mg_3Bi_2 phase begins to precipitate, and the $\text{Mg}_{17}\text{Al}_{12}$ phase appears at 200 ± 5 °C. The precipitation temperature gap between these two phases is more than 100 °C, which means that the composition can be effectively controlled by heat treatment.

Fig. 2 is the SEM images of the longitudinal section of the TRCed Mg alloys, mainly observing the segregation range in the central area. During the twin-roll casting process of the Mg alloy, the remaining solute rich liquid accumulates in the center and forms center line segregation along the RD. It is clear to identify the central segregation in bright white in both alloys but the morphology of the segregated phase changes with various alloying elements. For instance, the segregation phase in AZ31 alloys appears in the form of an uneven continuous block, while in AB31 is relatively smooth. The central segregation of AZ31 alloys is large and thick but changes into slender and discontinuous distribution in AB31 alloy. The enlarged matrix in yellow shows that both TRCed alloys are dendrite structures with almost free of second phases distribution at the grain boundary (GB). To dissolve such segregation and improve the subsequent plastic deformation ability, the TRCed alloys are homogenized at 450 °C for 12 h, and the SEM images of T4-treated alloys are shown in Fig. 3(c–d). After homogenization, the dendric morphology is completely eliminated, and the grains gradually grow into

equiaxed crystals. This is because the thermal deformation process alloy produces the deformation stored energy, which releases the storage energy in the solid solution stage, providing the driving force for the growth of the grain. Except coarsening of grain, the segregation in AZ31 alloys can be removed completely, and the β particles with low melting points dissolved into the matrix. Furthermore, the center-line segregation of AB31 alloys basically changed from a continuous block morphology to a non-continuous distribution at GBs. Meanwhile, lots of particles in the grain and at GB can be found.

Fig. 3 shows the XRD profile of the Mg alloys. According to the results, According to the diffraction results, the AZ31 alloy is mainly composed of α -Mg, $\text{Mg}_{17}\text{Al}_{12}$ phase, and the AB31 alloy consists of α -Mg, $\text{Mg}_{17}\text{Al}_{12}$, and Mg_3Bi_2 phase. The peak intensity of both the $\text{Mg}_{17}\text{Al}_{12}$ and Mg_3Bi_2 phases after homogenization is gradually weakening from originally TRCed samples agreed well with SEM observation, implying that the center line segregation eliminating.

To further confirm the improvement of central segregation with Bi addition, the element distribution was tested by the EPMA. As shown in Fig. 4(a–b), the main TRC sheets clearly represented that Al, Zn, and Bi elements were segregated. After homogenization (see Fig. 4(c–d)), no obvious central segregation in AZ31 alloys but a few thermal stable Mg_3Bi_2 phases remained due to its high melt point in AB31 alloy [31].

Clearly, the addition of Bi has a positive effect of inhibiting segregation in Mg–Al alloy. Hideyuki Tachi et al. [29] calculated amounts of segregation at GBs of Mg-0.05 at%X (X = Al, Bi, Ca, Ce, Gd, Nd, Y, Zn, Zr) alloys using the Hillert's grain boundary phase model and the trend of GB segregation of nine alloys are the same, in particular, the Al, Gd, Bi, and Zr showed lower segregation tendency. Zhou et al. [30] used the first-principle calculation to compute the temperature-dependent dilute tracer diffusion coefficients for 47 substitutional alloying elements in Mg and found that the diffusion coefficient of Zn is much higher than that of Bi. Therefore, after T4-treatment, the network-like $\text{Mg}_{17}\text{Al}_{12}$ phases have been basically eliminated, while in the case of AB31 alloy, a large number of Mg_3Bi_2 phases dispersed in the α -Mg matrix. The density of states (DOS) calculation also demonstrated that higher stability of Mg_3Bi_2 results from more bond electrons below the Fermi level [33,34].

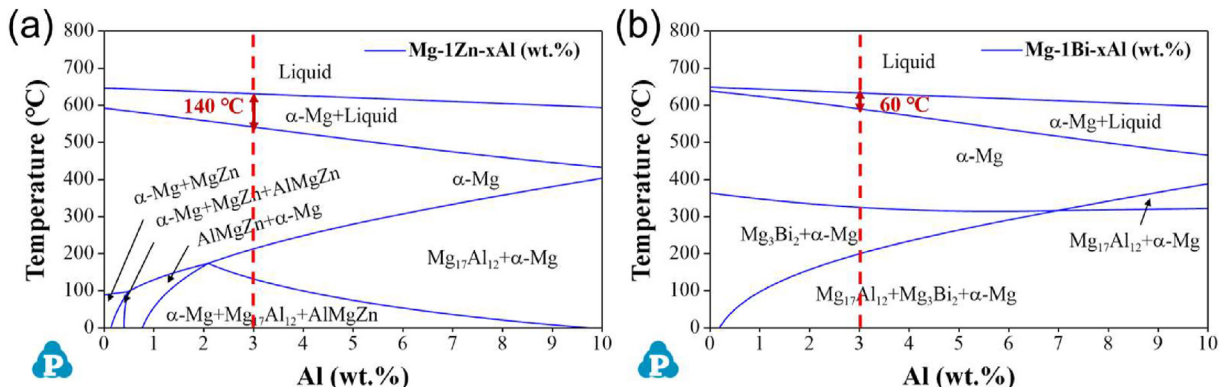


Fig. 1 – Equilibrium phase diagram predicted by Pandat™: (a) AZ31; (b) AB31.

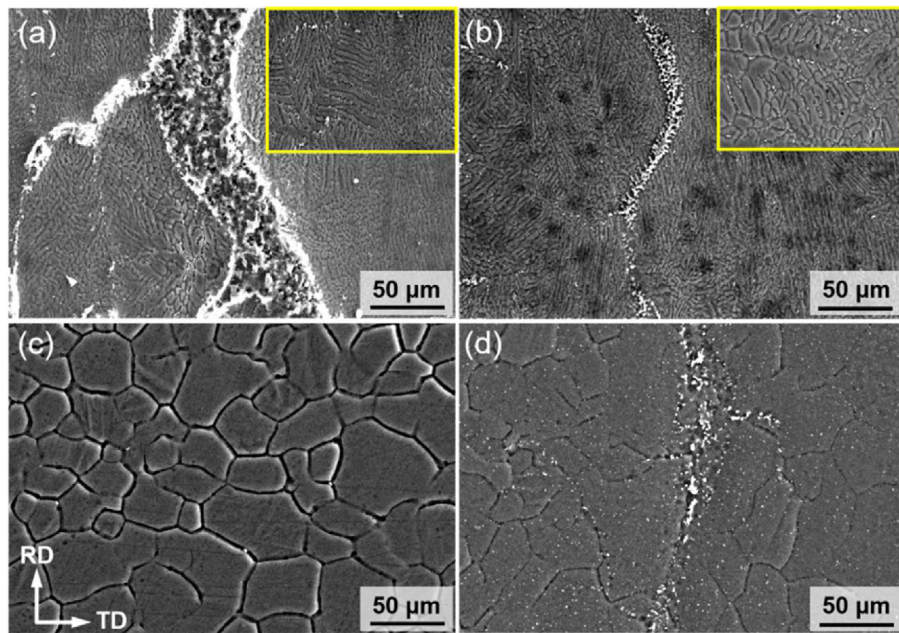


Fig. 2 – SEM images of twin-roll casted and homogenized AZ31 and AB31 alloys: (a) TRC-AZ31; (b) TRC-AB31; (c) T4-AZ31; (d) T4-AB31.

The OM and SEM images of as-rolled AZ31 and AB31 alloys are shown in Fig. 5. The profuse deformation twins can be found in the as-rolled AZ31 alloy. The addition of Bi plays an important role in refining the grains of as-rolled Mg alloys. Compared with AZ31 alloy, the grains of AB31 alloy are smaller and the fraction of DRX is significantly increased. Thus, a large number of fine equiaxed grains around a few coarse grains can be identified easily. It is speculated that the addition of Bi may promote the DRX process of as-rolled Mg alloys. In addition, there are no second particles exist in the as-rolled AZ31 strips (see Fig. 5 (c)), which due to the dissolving of Al into the matrix. However, during the multi-pass rolling of AB31 alloy, the insoluble large size particles after

homogenization are broken as well as small size dynamic precipitates were also generated and analyzed using TEM.

Fig. 6 shows the bright-field TEM images of the as-rolled AB31 strips along the [0001] and [11̄20]. Fig. 6(a–b) shows that the precipitates are nearly elliptical and clubbed in shape, which are Mg_3Bi_2 phases verified by SAED and EDX, i.e. These precipitates are in various scales with large size phases from broken bulk Mg_3Bi_2 particles and tiny size precipitates from dynamical precipitation. At present, it is generally believed that precipitates will affect the nucleation and growth process of DRX. Generally, dislocation accumulation and nucleation near the second particle usually promote DRX, which in turn, fine recrystallized grains are distributed closely to the

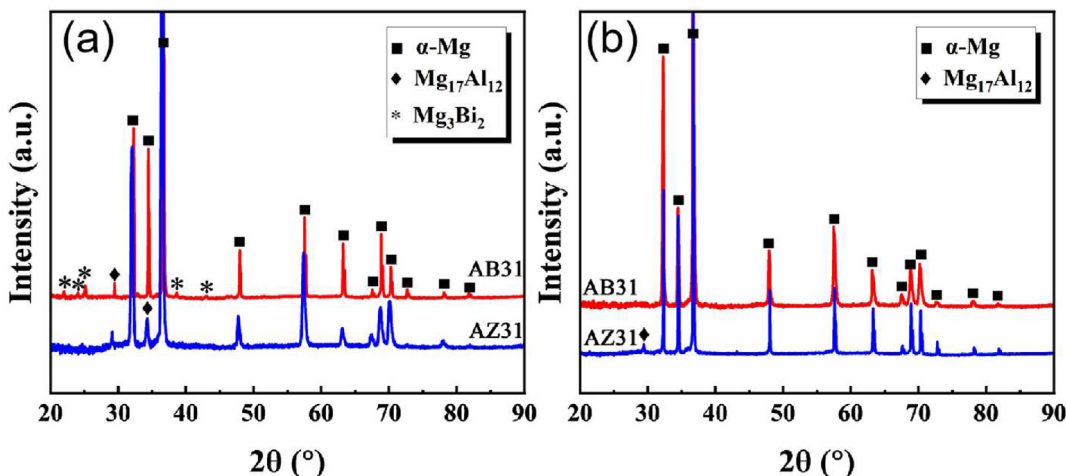


Fig. 3 – XRD results of (a) twin-roll casting and (b) homogenized AZ31 and AB31 alloys.

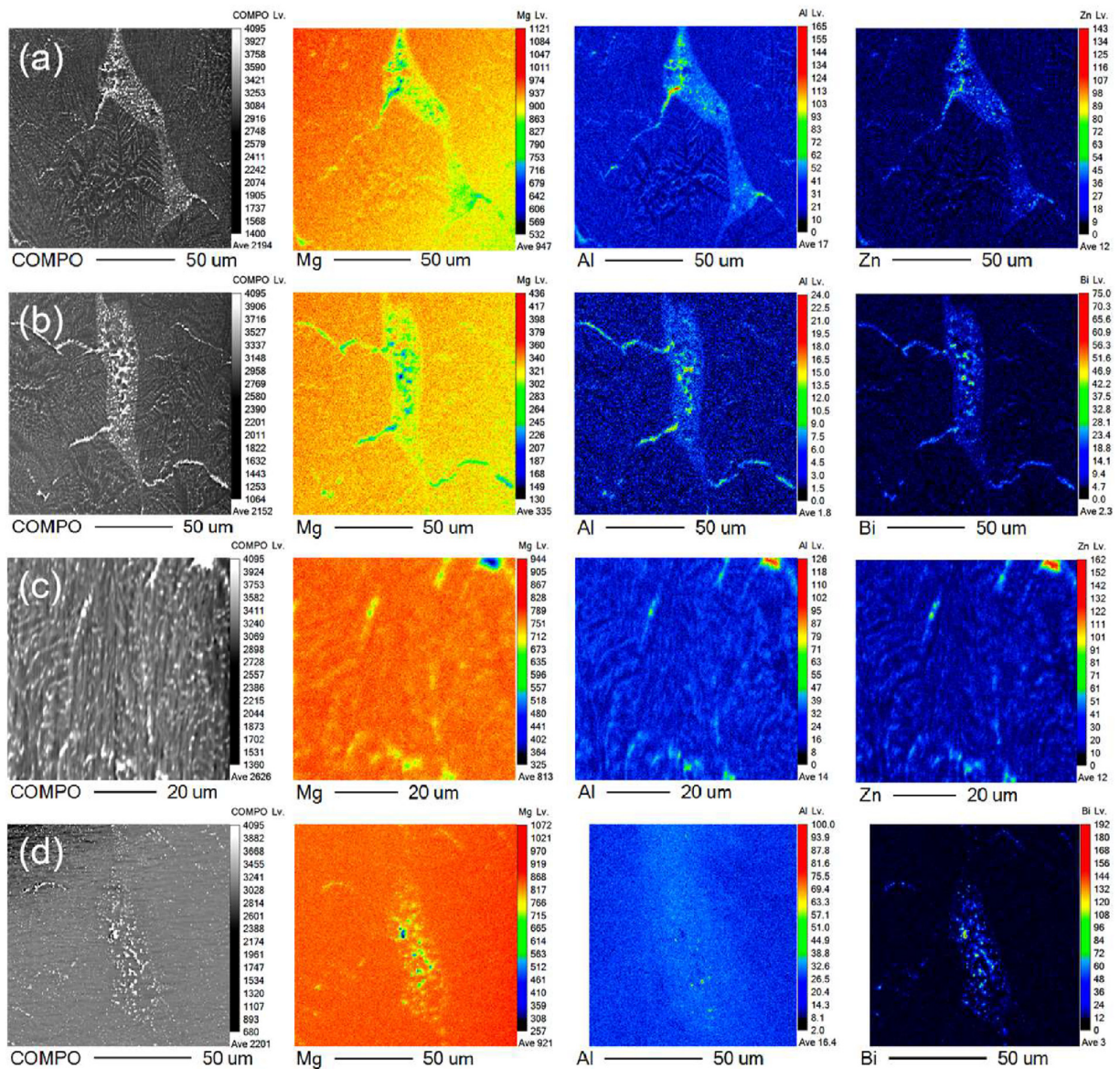


Fig. 4 – The EPMA images showing elements distribution in the center line segregation region of twin-roll casted and homogenized AZ31 and AB31 alloys: (a) TRC-AZ31; (b) TRC-AB31; (c) T4-AZ31; (d) T4-AB31.

particles, while particle free region is occupied by coarse uncrystallized grains. According to the particle stimulated nucleation (PSN) effect [35], the particles larger than 1 μm can be used as nucleation sites to promote the DRX. According to Fig. 6(c–d), Mg_3Bi_2 particles are observed along the grain boundary with an average grain size of 0.71 μm . Moreover, high dislocation stacking is observed in the area around the precipitated particles, which is necessary for DRX nucleation.

3.2. Texture evolution with DRX

Fig. 7(a–b) represents the EBSD results of the as-rolled alloys. The average grain size of the as-rolled AZ31 and AB31 strips is 9.75 μm and 8.79 μm , respectively. Consistent with OM observation, the addition of Bi elements exhibits grain refine-

effect. According to the inverse pole figures (IPF), the AZ31 alloys consist of twins, coarse grains, and DRX grains, which also coincide with SEM images. The black and white lines in IPF maps mean the low-angle grain boundaries (LAGBs: 2–10°) and high-angle grain boundaries (HAGBs: > 10°). The grain size of AB31 alloys is mainly concentrated in the fine grain region with an obvious peak in the range of 1–10 μm . Most deformed grains are display in red and DRXed grains are in blue and green, which indicates that the coarse grains show a relatively strong {0001} basal texture.

The statistic of DRX fraction (f_{DRX}) of as-rolled AZ31 and AB31 alloys are shown in Fig. 8(a–b). The f_{DRX} of the AZ31 and AB31 alloys are 31% and 41%, respectively. Compared with AZ31 alloy, the addition of Bi element improves the DRX fraction, which may be caused by the fine Mg_3Bi_2 particles

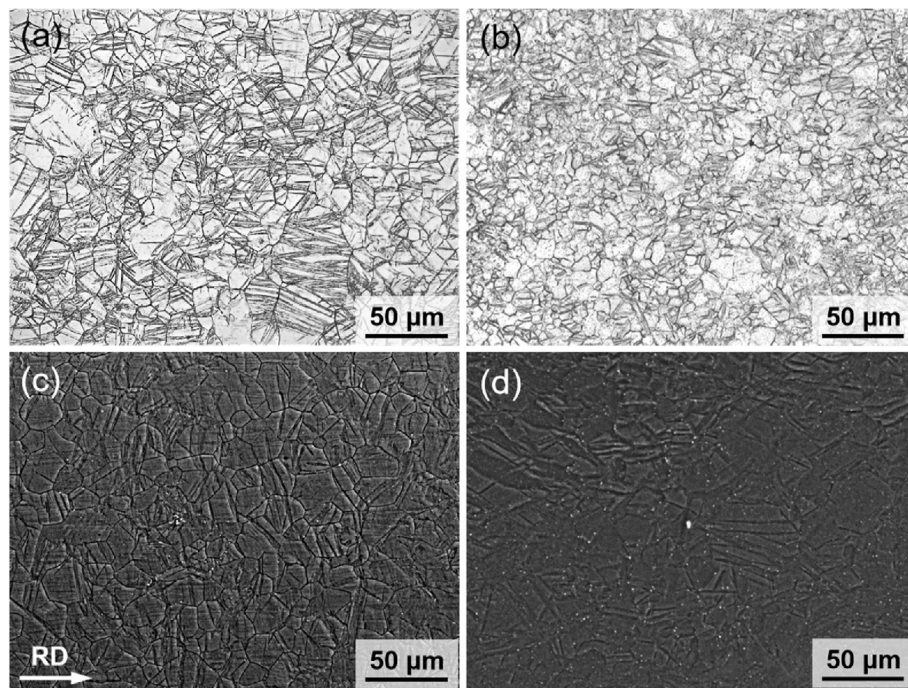


Fig. 5 – (a–b) OM and (c–d) SEM images of as-rolled (a, c) AZ31 and (b, d) AB31 alloys.

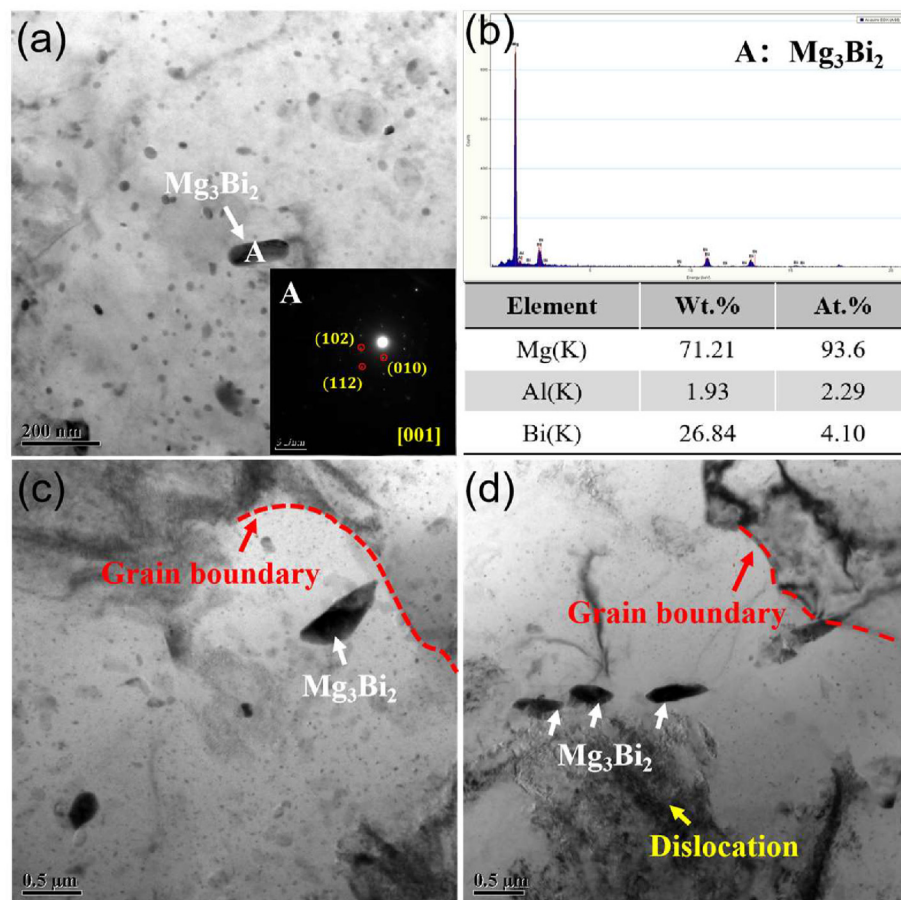


Fig. 6 – (a,c,d) Bright field images and (b) corresponding EDX results of as-rolled AB31 alloy.

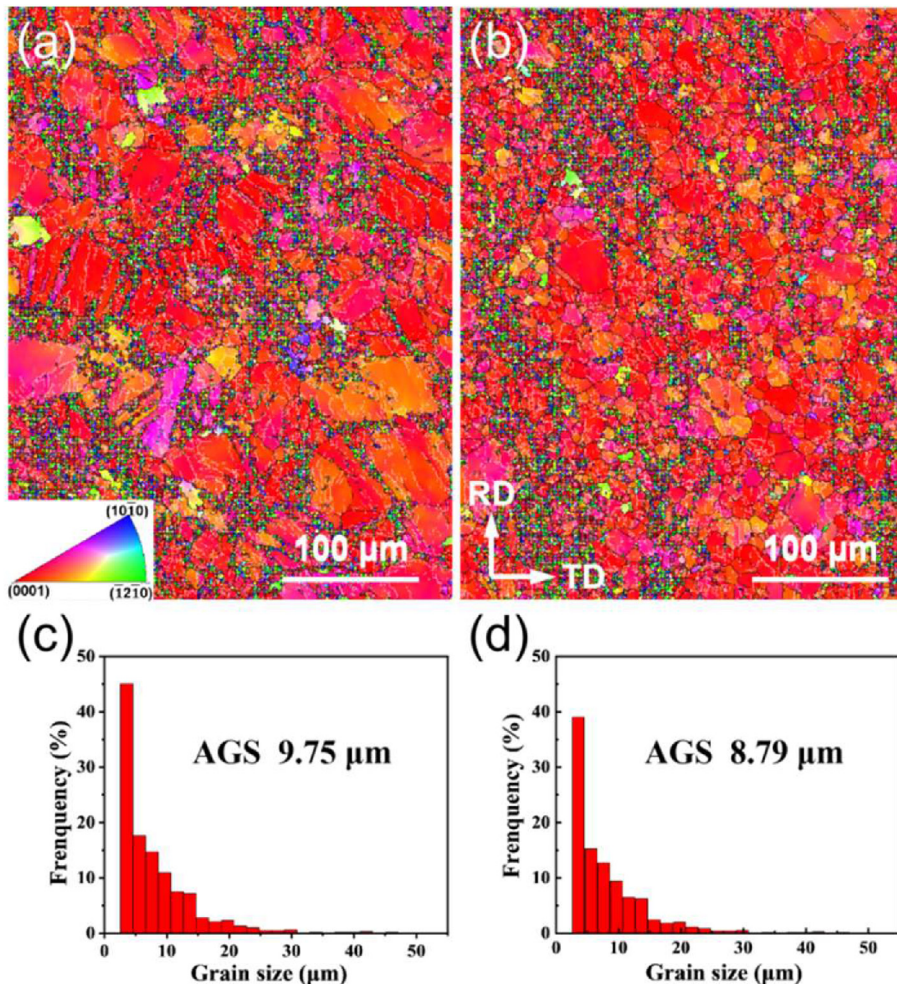


Fig. 7 – Inverse pole figures of as-rolled (a, c) AZ31 and (b, d) AB31 alloy with corresponding average grain size (AGS).

precipitated in AB31 alloy as the nucleation site during hot rolling and promoted the DRX. According to the misorientation analysis, the highest peaks of both curves appear in LAGBs and the peak value of AB31 alloys is lower. Due to Mg alloys with low stacking fault energy (SFE), the higher

dislocation density of the sub-grain boundary will result in easy migration and gradually change into the HAGBs. So, the recrystallized nucleation occurs through the sub-grain migration in AB31 alloy. On the one hand, as seen in Figs. 7 and 8, a large number of fine DRX grains are decorated near

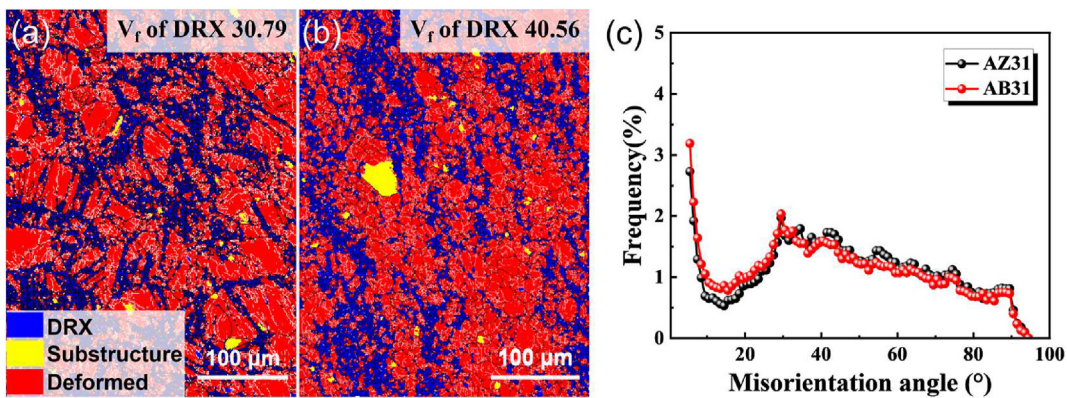


Fig. 8 – Volume fraction (V_f) of DRX of as-rolled (a) AZ31 and (b) AB31 alloy, (c) corresponding misorientation map.

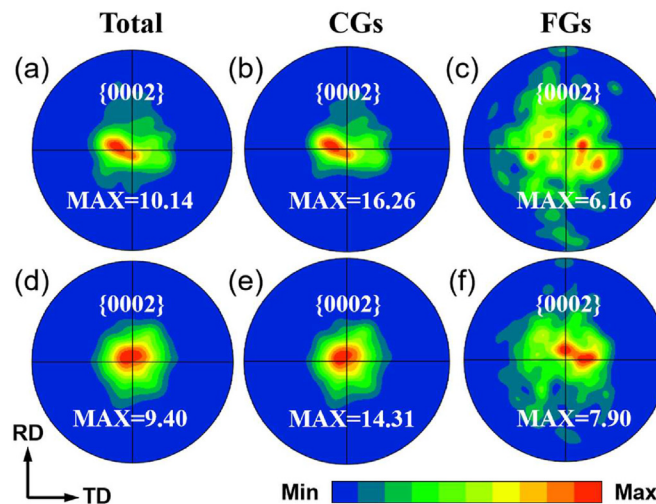


Fig. 9 – IPF of the as-rolled magnesium alloys (a–c) AZ31 (d–f) AB31.

the coarse particles in AB31 alloy, which means the particles boost DRX through PSN. On the other hand, Gibbs free energy (GFE) calculation manifests that the Gibbs energy of Mg_3Bi_2 is less than that of $Mg_{17}Al_{12}$ in the range of 298–548 K, so the dynamically precipitated Mg_3Bi_2 can be introduced at 250 °C [32]. According to Zener drag theory [7], the stable second phase can pin the GB of DRXed grains, which hinders the growth of these grains. Therefore, the grain size distribution of AB31 alloy is consistent with the previously reported results [35,36].

Fig. 9(a–b) shows the {0001} pole figures of HR-AZ31 and HR-AB31 alloy. The maximum texture intensity located in the center means that most grains are parallel to the RD, showing a typical strong basal texture. The addition of Bi reduces the basal texture intensity a little bit (~7.3% drop). The basal texture of the coarse and fine crystal regions were calculated, respectively. The results are shown in Fig. 9(c–f). The large deformed grains are mainly parallel to the processing direction, showing strong basal texture characteristics (Fig. 9(c–d)) with high texture strength value (max = 16.26, max = 14.31). The fine recrystallized grains show a bimodal texture that is weakened (max = 6.16, max = 7.90), indicating that the recrystallized grains are beneficial to weaken the matrix texture of magnesium alloy. Combined with some early reports [28,29], the weakening of the texture of AB31 alloy may be related to the increased f_{DRX} . With the increase of DRX, the number of deformed grains parallel to the basal plane decreases. It can be seen from Fig. 8 that the DRX fraction of AB31 alloys has increased by about 10%, thus newly DRX can weaken the basal texture to a certain extent. This relationship has been proved in Mg-Al [38], Mg-Zn [39], and Mg-Re [40,41] alloy systems.

Previous studies have shown that TD expansion may be attributed to prismatic $\langle a \rangle$ dislocation slip, and pyramidal $\langle c+a \rangle$ dislocation slip is considered to be the source of RD expansion activation [37]. The distribution of AB31 alloys along the TD direction has expanded, indicating that the stress increases in the TD direction.

3.3. Mechanical properties

The mechanical properties of the twin-roll casting and hot-rolled materials are summarized in Table 2. The UTS, YS, and El. of the TRC-AZ31 sheets are 264 MPa, 172 MPa, and 6.3%, respectively. When 1 wt.% Bi was added instead of Zn, the strength and elongation of the sheets decreased. After hot rolling, the elongation of AZ31 sheets is increased by about 50% without strength degradation. And the UTS and YS of HR-AB31 (UTS: 294 MPa, YS: 240 MPa) increased by 45% and 40%, respectively compared with the TRCed counterparts. In addition, the elongation of AB31 sheets increased to about 5.4%. The mechanical property enhancement of AB31 strips is mainly due to the synergistic effect of grain refinement and dispersion strengthening. Here, the refined grain contribution to strength can be calculated by the well-known Hall-Petch equation [40]:

$$\Delta\sigma = kd^{-1/2} \quad (1)$$

where d represents the average grain size, and k is the Hall-Petch constant ($k = 0.29 \text{ MPa m}^{1/2}$). On account of Eq. (1), the contribution of grain boundary strengthening calculated is 93 MPa and 98 MPa respectively. Thus, more strength contribution from precipitate strengthening can be expected. During the rolling, the precipitated Mg_3Bi_2 phases are broken into fine particles and dispersed homogeneously in the matrix (see Figs. 5 (d) and Fig. 6 (d)), which hinder the movement of dislocations to improve the strength of AB31 alloy. Furthermore,

Table 2 – Tensile properties of Mg sheets by various processing.

Sample	UTS (MPa)	YS (MPa)	El. (%)
TRC-AZ31	263.7	171.8	6.3
TRC-AB31	202.5	157.2	3.6
HR-AZ31	263.9	198.8	9.3
HR-AB31	293.6	240.3	5.4

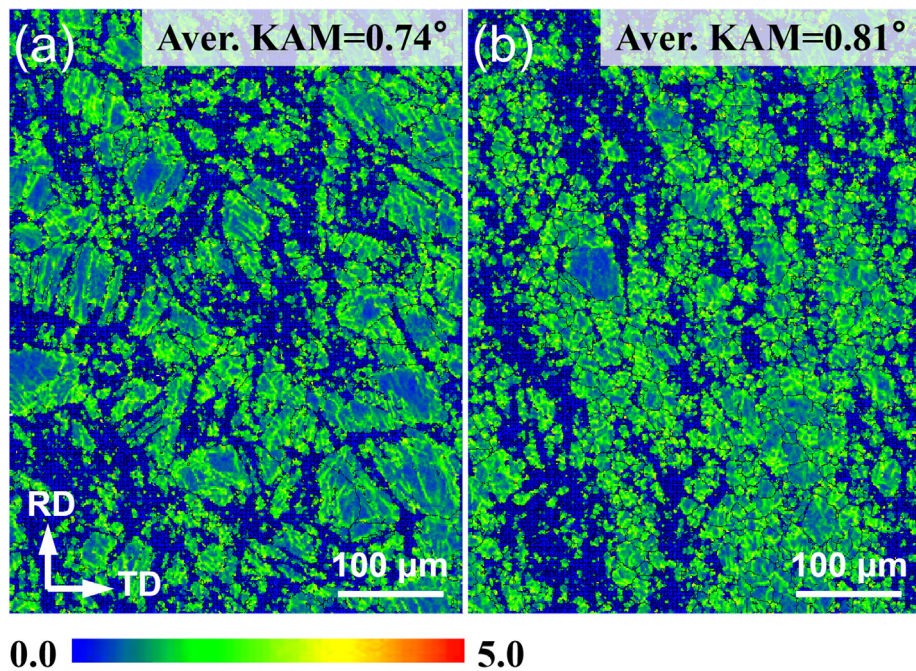


Fig. 10 – The kernel average misorientation (KAM) maps of as-rolled (a) AZ31 and (b) AB31 alloys.

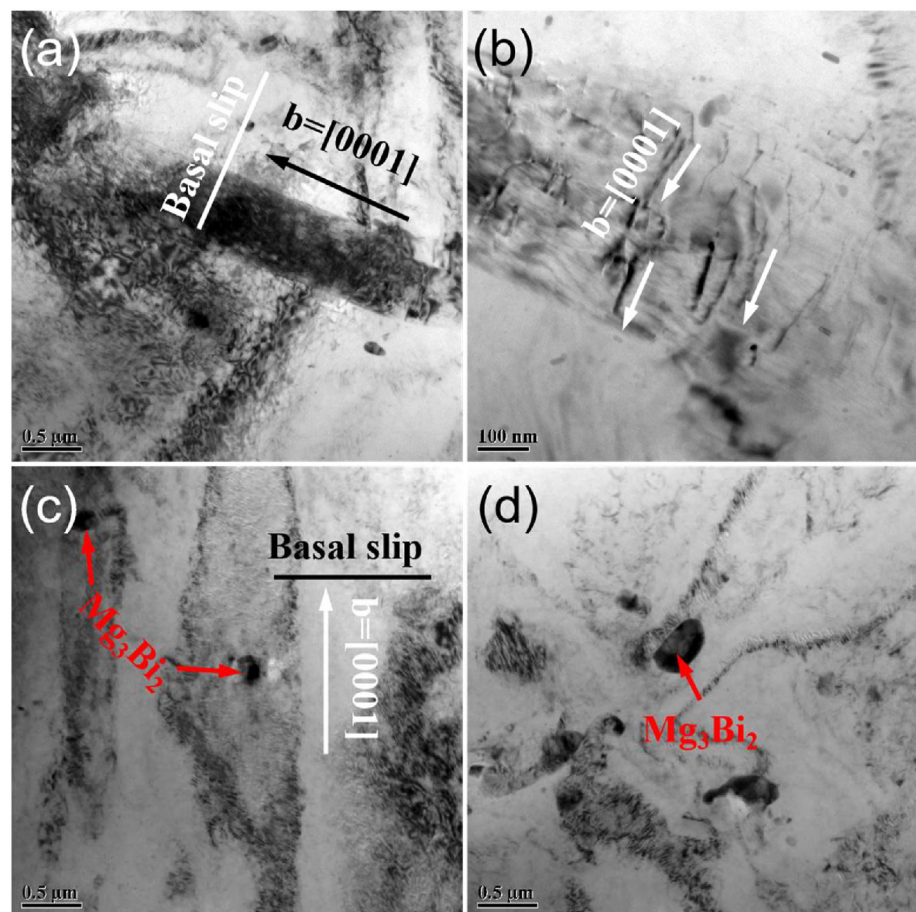


Fig. 11 – TEM micrographs of as-rolled AB31 alloys shown (a, b) dislocations and (c, d) precipitates.

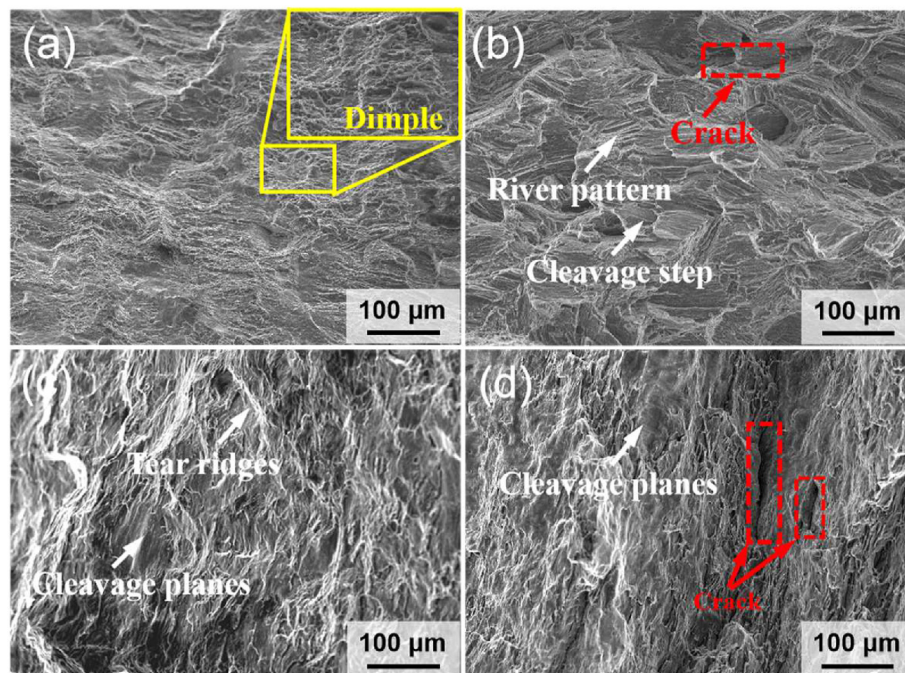


Fig. 12 – Fracture surface of twin-roll casting and as-rolled AZ31 and AB31 alloys: (a) TRC-AZ31; (b) TRC-AB31; (c) HR-AZ31; (d) HR-AB31.

a large amount of Bi remains as solute atoms in AB31 alloy after rolling at 250 °C, and the undissolved Bi will lead to partial solid solution strengthening.

The addition of Bi can also enhance strain hardening and help to improve strength. Fig. 10 gives the kernel average misorientation (KAM) maps of the as-rolled alloys and the KAM values of AZ31 and AB31 alloys are 0.74 and 0.81, respectively. The difference between KAM average value is attributed to the dislocation proliferation and accumulation. According to the dislocation strengthening theory, the dislocation and precipitate interaction can control the extent of strengthening during plastic deformation. As shown in Fig. 11 (a), the accumulation and entanglement of dislocations in AB31 alloy leads to increased dislocation number density, enhanced work hardening, and reduced ductility. As shown in Fig. 11 (b), it can be seen that the $\langle c + a \rangle$ is activated in AB31 alloy. The dislocation pinned by the Mg_3Bi_2 phase can delay the recovery of dislocation, resulting in the further improvement of dislocation energy storage capacity and improvement of strength.

Fig. 12 shows the SEM of fractured tensile specimens of twin-roll casting (TRC) and hot-rolling (HR) alloys. Many dimples and few cleavage planes are observed in TRC-AZ31 alloys, indicating that the fracture mechanism is a ductile-brittle mixed fracture. The tensile fractography of TRC-AB31 alloys shows obviously cleavage planes and river patterns. And few small cracks and dimples are also observed, which indicates that the fracture mechanism of TRC-AB31 alloys is a quasi-cleavage fracture. The fracture surface of both HR-AZ31 and HR-AB31 alloys is similar, and the cleavage planes and tear edges can be found. In addition, some cracking also engenders in HR-AB31 alloys indicating worse elongation. A large number of brittle second phases in AB31

alloys, which reported to act as cracking initiation during loading [30].

4. Conclusion

In this study, we compared the microstructure and mechanical properties of Mg–3Al–1Zn alloy and new Mg–3Al–1Bi alloy are fabricated by twin roll casting and hot rolling. The addition of Bi shows the following positive influences on Mg–3Al alloy.

- (1) The improvement of serious central segregation in TRC evaluated by phase diagram calculation and EPMA analysis due to the high solidification temperature and narrow solidification range;
- (2) More refined grain size can be obtained and the high thermal stable Mg_3Bi_2 particles introduced can not only affect DRX behavior through the PSN effect but also refine the microstructure by pinning GBs;
- (3) The significant enhancement of UTS and YS in as-rolled AB31 alloy is mainly due to dispersion strengthening. However, the brittle Mg_3Bi_2 as a cracking source leads to the deterioration of elongation.

Declaration of Competing Interest

The authors declare that they have no known competing financial interests or personal relationships that could have appeared to influence the work reported in this paper.

Acknowledgement

This work was supported by the National Natural Science Foundation of China [grant number 51701060], the Hebei province [grant number E2022202158]; and the foundation of strengthening program [grant number 2019-JCJQ-142-00].

REFERENCES

- [1] Wu G, Wang C, Sun M, Ding W. Recent developments and applications on high-performance cast magnesium rare-earth alloys. *J Magnes Alloys* 2021;9(1):1–20. <https://doi.org/10.1016/j.jma.2020.06.021>.
- [2] Hirsch J, Al-Sammam T. Superior light metals by texture engineering: optimized aluminum and magnesium alloys for automotive applications. *Acta Mater* 2013;61(3):818–43. <https://doi.org/10.1016/j.actamat.2012.10.044>.
- [3] Liu LX, Yang DL, Li XL, Hu SW. Mechanical properties, corrosion resistance and biocompatibilities of degradable Mg-RE alloys: a review. *J Mater Res Technol* 2019;8(1):1538–49. <https://doi.org/10.1016/j.jmrt.2018.08.003>.
- [4] Jiao ZY, Lyu SY, Wang L, You C, Chen MF. Improving the mechanical properties and corrosion resistance of biodegradable Mg-Zn-Ca-Mn alloy bone screw through structural optimization. *J Mater Res Technol* 2022;21:1442–53. <https://doi.org/10.1016/j.jmrt.2022.10.004>.
- [5] Wang Y, Kang SB, Cho J. Microstructural evolution of twin-roll cast Mg-3Al-0.5Mn-0.2Mm alloys during warm rolling and subsequent annealing. *J Mater Process Technol* 2010;210(10):1270–5. <https://doi.org/10.1016/j.jmatprotec.2010.03.013>.
- [6] Bae JH, Shim MS, Suh BC, Kim DW, Park SH, Kim NJ. Segregation in twin-roll cast Mg alloy and its suppression through alloy design. *Mater Lett* 2014;132:361–4. <https://doi.org/10.1016/j.matlet.2014.06.113>.
- [7] Wang Y, Kang SB, Cho J. Microstructure and mechanical properties of Mg-Al-Mn-Ca alloy sheet produced by twin roll casting and sequential warm rolling. *J Alloys Compd* 2011;509(3):704–11. <https://doi.org/10.1016/j.jallcom.2010.07.183>.
- [8] Alaneme KK, Okotete EA. Enhancing plastic deformability of Mg and its alloys-A review of traditional and nascent developments. *J Magnes Alloys* 2017;5(4):460–75. <https://doi.org/10.1016/j.jma.2017.11.001>.
- [9] Beyerlein IJ, Tóth LS. Texture evolution in equal-channel angular extrusion. *Prog Mater Sci* 2009;54(4):427–510. <https://doi.org/10.1016/j.pmatsci.2009.01.001>.
- [10] Dogan E, Vaughan MW, Wang SJ, Karaman I, Proust G. Role of starting texture and deformation modes on low-temperature shear formability and shear localization of Mg-3Al-1Zn alloy. *Acta Mater* 2015;89:408–22. <https://doi.org/10.1016/j.actamat.2014.12.006>.
- [11] Silva CLP, Soares RP, Pereira PHR, Figueiredo RB, Lins VFC, Langdon TG. The effect of high-pressure torsion on microstructure, hardness and corrosion behavior for pure magnesium and different magnesium alloys. *Adv Eng Mater* 2019;21(3). <https://doi.org/10.1002/adem.201801081>.
- [12] Mikhaylovskaya AV, Kotov AD, Kishchik MS, Prosviryakov AS, Portnoy VK. The effect of isothermal multi-directional forging on the grain structure, superplasticity, and mechanical properties of the conventional Al-Mg-based alloy. *Metals* 2019;9(1). <https://doi.org/10.3390/met 9010033>.
- [13] Yu J, Liao HX, Lee JH, Moon YH, Yoon HS, Kim J, et al. Microstructural evolution of multi-pass caliber-rolled Mg-Sn and Mg-Sn-Mn alloys. *Metals* 2020;10(9). <https://doi.org/10.3390/met1009 1203>.
- [14] Kwak BJ, Park SH, Moon YH, Lee JH, Lee TK. Plastic anisotropy of multi-pass caliber-rolled Mg alloy with split texture distribution. *Mater Sci Eng, A* 2020;788. <https://doi.org/10.1016/j.msea.2020.139496>.
- [15] Zeng ZR, Stanford N, Davies CHJ, Nie JF, Birbilis N. Magnesium extrusion alloys: a review of developments and prospects. *Int Mater Rev* 2018;64(1):27–62. <https://doi.org/10.1080/09506608.2017.1421439>.
- [16] Du Y-Z, Zheng MY, Jiang BL. Comparison of microstructure and mechanical properties of Mg-Zn microalloyed with Ca or Ce. *Vacuum* 2018;151:221–5. <https://doi.org/10.1016/j.vacuum.2018.02.029>.
- [17] Griffiths D. Explaining texture weakening and improved formability in magnesium rare earth alloys. *Mater Sci Technol* 2014;31(1):10–24. <https://doi.org/10.1179/1743284714Y.0000000632>.
- [18] Kamrani S, Fleck C. Effects of calcium and rare-earth elements on the microstructure and tension-compression yield asymmetry of ZEK100 alloy. *Mater Sci Eng, A* 2014;618:238–43. <https://doi.org/10.1016/j.msea.2014.09.023>.
- [19] Bohlen J, Nürnberg MR, Senn JW, Letzig D, Agnew SR. The texture and anisotropy of magnesium-zinc-rare earth alloy sheets. *Acta Mater* 2007;55(6):2101–12. <https://doi.org/10.1016/j.actamat.2006.11.013>.
- [20] Chino Y, Sassa K, Mabuchi M. Tensile properties and stretch formability of Mg-1.5 mass%-0.2 mass% Ce sheet rolled at 723 K. *Mater Trans* 2008;49(7):1710–2. <https://doi.org/10.2320/matertrans.MEP2008136>.
- [21] Yuasa M, Miyazawa N, Hayashi M, Mabuchi M, Chino Y. Effects of group II elements on the cold stretch formability of Mg-Zn alloys. *Acta Mater* 2015;83:294–303. <https://doi.org/10.1016/j.actamat.2014.10.005>.
- [22] She J, Pan F, Zhang J, Tang A, Luo S, Yu Z, et al. Microstructure and mechanical properties of Mg-Al-Sn extruded alloys. *J Alloys Compd* 2016;657:893–905. <https://doi.org/10.1016/j.jallcom.2015.10.146>.
- [23] Park SH, Jung JG, Kim YM, You BS. A new high-strength extruded Mg-8Al-4Sn-2Zn alloy. *Mater Lett* 2015;139:35–8. <https://doi.org/10.1016/j.matlet.2014.10.033>.
- [24] Go J, Lee JU, Yu H, Park SH. Influence of Bi addition on dynamic recrystallization and precipitation behaviors during hot extrusion of pure Mg. *J Mater Sci Technol* 2020;44:62–75. <https://doi.org/10.1016/j.jmst.2019.10.036>.
- [25] Sasaki TT, Ohkubo T, Hono K. Precipitation hardenable Mg-Bi-Zn alloys with prismatic plate precipitates. *Scripta Mater* 2009;61(1):72–5. <https://doi.org/10.1016/j.scriptamat.2009.03.015>.
- [26] Jun JH, Lee MH. Effect of Bi addition on thermal stability and tensile ductility of Mg-3%Zn-0.4%Zr alloy. *Mater Sci Forum* 2010;654–656:647–50. <https://doi.org/10.4028/www.scientific.net/MSF.654-656.647>.
- [27] Huang Z, Liu W, Qi WJ, Xu J, Zhou N. Effects of Bi on the microstructure and mechanical property of ZK60 alloy. *J Magnes Alloys* 2015;3(1):29–35. <https://doi.org/10.1016/j.jma.2014.12.005>.
- [28] Liu P, Jiang H, Cai Z, Kang Q, Zhang Y. The effect of Y, Ce and Gd on texture, recrystallization and mechanical property of Mg-Zn alloys. *J Magnes Alloys* 2016;4(3):188–96. <https://doi.org/10.1016/j.jma.2016.07.001>.
- [29] Tachi H, Suzuki K, Huang X, Tsukada Y, Koyama T, Chino Y. Relationship between calculated segregation, texture and room temperature formability of binary magnesium alloys. *J Jpn Inst Metals* 2021;85(10):382–90. <https://doi.org/10.2320/jinstmet.J2021007>.
- [30] Zhou BC, Shang SL, Wang Y, Liu ZK. Diffusion coefficients of alloying elements in dilute Mg alloys: a comprehensive first-

- principles study. *Acta Mater* 2016;103:573–86. <https://doi.org/10.1016/j.actamat.2015.10.0103>.
- [31] Zhou DW, Liu JS, Xu SH, Peng P. Thermal stability and elastic properties of Mg_3Sb_2 and Mg_3Bi_2 phases from first-principles calculations. *Phys B* 2010;405(13):2863–8. <https://doi.org/10.1016/j.physb.2010.04.013>.
- [32] Jiang L, Huang GJ, Godet S, Jonas JJ, Luo AA. Particle-stimulated nucleation of dynamic recrystallization in AZ31 alloy at elevated temperatures. *Mater Sci Forum* 2005;488–489:261–4. <https://doi.org/10.4028/www.scientific.net/MSF.488-489.261>.
- [33] Meng SJ, Yu H, Zhang H, Cui H, Park SH, Zhao W, et al. Microstructure and mechanical properties of an extruded Mg-8Bi-1Al-1Zn (wt%) alloy. *Mater Sci Eng, A* 2017;690:80–7. <https://doi.org/10.1016/j.msea.2017.02.095>.
- [34] Li X, Qi W. Effect of initial texture on texture and microstructure evolution of ME20 Mg alloy subjected to hot rolling. *Mater Sci Eng, A* 2013;560:321–31. <https://doi.org/10.1016/j.msea.2012.09.074>.
- [35] Li X, Jiao F, Al-Sammam T, Ghosh Chowdhury S. Influence of second-phase precipitates on the texture evolution of Mg-Al-Zn alloys during hot deformation. *Scripta Mater* 2012;66(3–4):159–62. <https://doi.org/10.1016/j.scriptamat.2011.10.028>.
- [36] Xia N, Wang C, Gao YP, Hua ZM, Zha M, Wang HY, et al. Enhanced ductility of Mg-1Zn-0.2Zr alloy with dilute Ca addition achieved by activation of non-basal slip and twinning. *Mater Sci Eng, A* 2021;813. <https://doi.org/10.1016/j.msea.2021.141128>.
- [37] Yi SB, Bohlen J, Sandlöbes S, Zaefferer S, Letzig D, Kainer KU. Microstructural evolution during recrystallization of magnesium alloys. *Mater Sci Forum* 2012;706–709:1291–6. <https://doi.org/10.4028/www.scientific.net/MSF.706-709.1291>.
- [38] Basu I, Al-Sammam T, Gottstein G. Shear band-related recrystallization and grain growth in two rolled magnesium-rare earth alloys. *Mater Sci Eng, A* 2013;579:50–6. <https://doi.org/10.1016/j.msea.2013.04.076>.
- [39] Wang PY, Wang BY, Wang C, Wang JG, Zha M, Wang HY, et al. Design of multicomponent Mg-Al-Zn-Sn-Bi alloys with refined microstructure and enhanced tensile properties. *Mater Sci Eng, A* 2020;791. <https://doi.org/10.1016/j.msea.2020.139696>.
- [40] Hansen N. Hall-Petch relation and boundary strengthening. *Scripta Mater* 2004;51:801–6. <https://doi.org/10.1016/j.scriptamat.2004.06.002>.
- [41] Cepeda-Jiménez CM, Castillo-Rodríguez M, Pérez-Prado MT. Origin of the low precipitation hardening in magnesium alloys. *Acta Mater* 2019;165:164–76. <https://doi.org/10.1016/j.actamat.2018.11.044>.
- [42] Yu H, Fan SD, Meng SJ, You BS, Shin KS. Microstructural evolution and mechanical properties of binary Mg-xBi ($x = 2, 5$, and 8wt%) alloys. *J. Magnes. Alloys* 2021;9(3):983–94. <https://doi.org/10.1016/j.jma.2020.03.015>.
- [43] Liang D, Cowley CB. The twin-roll strip casting of magnesium. *JOM* 2004;56(5):26–8. <https://doi.org/10.1007/s11837-004-0122-6>.